RSC Advances

PAPER

View Article Online
View Journal | View Issue

Cite this: *RSC Adv.*, 2018, **8**, 9879

Ce^{3+} and Tb^{3+} doped $Ca_3Gd(AlO)_3(BO_3)_4$ phosphors: synthesis, tunable photoluminescence, thermal stability, and potential application in white LEDs

Bin Li, Qi Sun, Shaoying Wang, Heng Guo and Xiaoyong Huang *

Novel blue-green-emitting $Ca_3Gd(AlO)_3(BO_3)_4$:Ce^{3+},Tb^{3+} phosphors were successfully synthesized *via* traditional high temperature solid reaction method. X-ray diffraction, luminescence spectroscopy, fluorescence decay time and fluorescent thermal stability tests have been used to characterize the as-prepared samples. The energy transfer from Ce^{3+} to Tb^{3+} ions in the $Ca_3Gd(AlO)_3(BO_3)_4$ host has been demonstrated to be by dipole–dipole interaction, and the energy transfer efficiency reached as high as 83.6% for $Ca_3Gd_{0.39}(AlO)_3(BO_3)_4$:0.01$Ce^{3+}$,0.6$Tb^{3+}$. The critical distance was calculated to be 9.44 Å according to the concentration quenching method. The emission colour of the obtained phosphors can be tuned appropriately from deep blue (0.169, 0.067) to green (0.347, 0.494) through increasing the doping concentrations of Tb^{3+}. Moreover, the $Ca_3Gd_{0.39}(AlO)_3(BO_3)_4$:0.01$Ce^{3+}$,0.6$Tb^{3+}$ phosphor possessed excellent thermal stability at high temperature, and the emission intensity at 423 K was about 87% of that at 303 K. Finally, the fabricated prototype LED device with a $BaMgAl_{10}O_7$:Eu^{2+} blue phosphor, $CaAlSiN_3$:Eu^{2+} red phosphor, $Ca_3Gd_{0.39}(AlO)_3(BO_3)_4$:0.01$Ce^{3+}$,0.6$Tb^{3+}$ green phosphor and 365 nm-emitting InGaN chip exhibited bright warm white light. The current study shows that $Ca_3Gd_{0.39}(AlO)_3(BO_3)_4$:0.01$Ce^{3+}$,0.6$Tb^{3+}$ can be used as a potential green phosphor for white LEDs.

Received 10th February 2018
Accepted 2nd March 2018

DOI: 10.1039/c8ra01322e

rsc.li/rsc-advances

1. Introduction

During the past decades, inorganic luminescent materials based on rare-earth (RE) ions have attracted many researchers' attention because of their wide applications, such as lighting, displays, lasers, solar cells, sensors and bioimaging.[1–19] For lighting, the research on phosphor-converted white light-emitting diodes (pc-WLEDs) is prevalent because they possess many merits, including low electricity consumption, long service life, small volume, non-pollution, and fast response.[20] RE ions can emit various different fascinating colours due to their special 4f shell configuration. Through combining different RE ions and controlling their respective concentration, the emission of phosphor can be tuned from violet to red.[21–37] Therefore, the use of different RE ions can produce a variety of colour tunable phosphors.[38–40] As one important part of RGB (red, green and blue) phosphors for ultraviolet (UV)-pumped WLEDs, green phosphors are always fabricated by Tb^{3+} ion as its intrinsic green emissions peaking at around 544 nm.[41] However, Tb^{3+} activated phosphors are inefficient because their absorption lines of 4f–4f spin-forbidden transitions are too weak. As a result, researchers introduce Ce^{3+} ions as a sensitizer to intensify Tb^{3+} ions absorption. Furthermore, the broad f–d absorption band of Ce^{3+} ions locate on UV region, which maximally broadens the application of Tb^{3+} ions.[42] But to successfully realize that, not only request Ce^{3+} and Tb^{3+} ions but also need a proper host that can influence RE ions luminescent properties.

Borates have been proved to be outstanding host materials for inorganic phosphors, because they have many advantages, including high chemical stability, good thermal stability, and low synthetic temperature.[43,44] Here in this work, we reported the luminescent properties of novel Ce^{3+} and Tb^{3+} co-activated $Ca_3Gd(AlO)_3(BO_3)_4$ phosphors. The crystal structure and the site substitution were investigated to verify the purity of phosphors and clarify the effect of doping on crystal structures. The luminescent performance including excitation, emission spectra, decay time, and chromaticity diagram was discussed to elucidate the luminescent mechanism of doping ions and the energy transfer mechanism between Ce^{3+} and Tb^{3+} in the $Ca_3Gd(AlO)_3(BO_3)_4$ host. Moreover, we examined their thermal stability and LED device performance for the practical application.

2. Experimental

A series of $Ca_3Gd_{(0.99-x)}(AlO)_3(BO_3)_4$:0.01$Ce^{3+}$,$xTb^{3+}$ (x = 0, 0.02, 0.05, 0.1, 0.2, 0.3, 0.4, 0.5 and 0.6) samples were successfully

Key Lab of Advanced Transducers and Intelligent Control System, Ministry of Education and Shanxi Province, College of Physics and Optoelectronics, Taiyuan University of Technology, Taiyuan 030024, PR China. E-mail: huangxy04@126.com

fabricated *via* a conventional high-temperature solid-state reaction technique. H_3BO_3 (analytical reagent), $CaCO_3$ (analytical reagent), Gd_2O_3 (99.99%), Al_2O_3 (analytical reagent), $Ce(NO_3)_3 \cdot 6H_2O$ (99.99%) and $Tb(NO_3)_3 \cdot 6H_2O$ (99.99%) were used as raw materials. According to the stoichiometric ratio, these raw materials were weighted and ground in an agate mortar to achieve uniformity. In order to compensate the volatilization, the amount of H_3BO_3 is in excess of 5 wt%. Then, these uniform mixtures were put in the alumina crucibles and sintered at 1100 °C for 4 h in CO atmosphere to reduce the Ce ion into tri-valence ion. After that, the furnace was cooled down naturally to room temperature, and the final products were ground and collected for further characterization.

The X-ray diffraction (XRD) patterns of the samples were recorded on a Bruker D8 X-ray diffractometer using Cu Kα radiation ranging with 5–80° at step rate of 0.02°. The morphology properties of the samples were obtained by a field-emission scanning electron microscope (FE-SEM; MAIA3 TESCAN). The room-temperature photoluminescence (PL) and PL excitation (PLE) spectra and luminescence decay lifetimes of phosphors were measured by Edinburgh FS5 spectrometer equipped with a 150 W continued-wavelength Xenon lamp and a pulsed Xenon lamp, respectively. Temperature-dependent PL spectra were recorded by using the same spectrophotometer and detectors equipped with a temperature controller. The internal quantum efficiency (IQE) of the phosphors was measured on an Edinburgh FS5 spectrometer equipped with an integrating sphere coated with $BaSO_4$.

The commercial blue phosphor $BaMgAl_{10}O_7:Eu^{2+}$, red phosphor $CaAlSiN_3:Eu^{2+}$ and our green phosphor $Ca_3Gd_{0.39}(AlO)_3(BO_3)_4:0.01Ce^{3+},0.6Tb^{3+}$ were mixed with silicone thoroughly, and the obtained phosphor–silicone mixture was coated on the surface of the LED chips to fabricate WLED device. The photoelectric properties of the fabricated devices were measured by using an integrating sphere spectroradiometer system (HAAS-2000, Everfine). The LEDs were operated at 3 V with various driven currents of 20, 60, 120, 180, 240 and 300 mA, respectively. The spectral power distributions of LEDs were measured using a corrected spectrometer to calculate their values of correlated colour temperature (CCT) and colour rendering index (CRI).

3. Results and discussion

3.1 Phase and structure

Fig. 1 shows the XRD patterns of $Ca_3Gd(AlO)_3(BO_3)_4$ and $Ca_3Gd_{0.39}(AlO)_3(BO_3)_4:0.01Ce^{3+},0.6Tb^{3+}$ phosphors. Obviously, the obtained patterns agreed well with $Ca_3Y(AlO)_3(BO_3)_4$, which can be found in Inorganic Crystal Structure Database (ICSD-172154), suggesting that the compounds were obtained as a single phase.

Based on the *iso*-structure of $Ca_3Y(AlO)_3(BO_3)_4$, the Rietveld refinements of the $Ca_3Gd(AlO)_3(BO_3)_4$ and $Ca_3Gd_{0.39}(AlO)_3(BO_3)_4:0.01Ce^{3+},0.6Tb^{3+}$ were performed to further analyze the crystal structure details, as shown in Fig. 2. It can be found that $Ca_3Gd(AlO)_3(BO_3)_4$ crystallized in a hexagonal unit cell with space group $P63/m$, which coincide with $Ca_3Y(AlO)_3(BO_3)_4$.

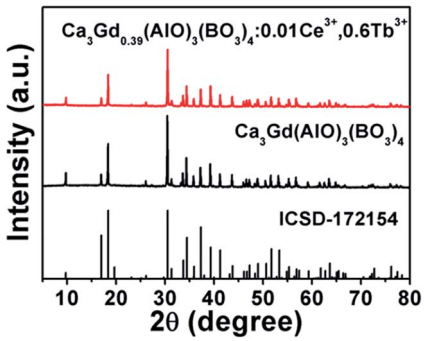

Fig. 1 XRD patterns of $Ca_3Gd_{0.39}(AlO)_3(BO_3)_4:0.01Ce^{3+},0.6Tb^{3+}$ and $Ca_3Gd(AlO)_3(BO_3)_4$ phosphors. The standard data of CYAB (ICSD-172154) was shown.

Moreover, crystallographic data and details were summarized in Table 1, and the refined lattice parameters are changed slightly through substituting Y^{3+}(1.075 Å) ions with Gd^{3+}(1.107 Å), Ce^{3+}(1.196 Å) and Tb^{3+}(1.095 Å) ions. It can be attributed to the different radii of these ions.[45]

The crystal structure of $Ca_3Gd(AlO)_3(BO_3)_4$ and coordination (CN) environments of Ca^{2+} sites (Ca1 and Ca2) are depicted in Fig. 3. Clearly, Ca2 sites are surrounded with ten oxygen atoms while Ca1 sites are coordinated with nine oxygen atoms, but the coordinative six oxygen (O4) ions of Ca2 are also shared by the adjacent four B ions. Therefore, the CN sites of Ca1 and Ca2 are 9 and 7, respectively. The above results suggest that Ln^{3+} (Gd^{3+}, Ce^{3+} and Tb^{3+}) ions prefer to occupy the Ca1 sites.[46]

Fig. 4(a) shows the representative FE-SEM image of $Ca_3Gd_{0.39}(AlO)_3(BO_3)_4:0.01Ce^{3+},0.6Tb^{3+}$ phosphors. As can be seen, the studied sample was made up of irregular and aggregated microparticles with the size ranging from 2 to 10 μm. Besides, the elemental mapping result revealed that the components of Ca, Ga, Al, O, B, Ce and Tb were uniformly distributed over the whole range of particles, as can be seen in Fig. 4(b).

3.2 Photoluminescence properties

Fig. 5(a) shows the PLE and PL spectra of $Ca_3Gd_{0.99}(AlO)_3(BO_3)_4:0.01Ce^{3+}$ phosphor. By monitoring at 402 nm, there were two principle excitation bands in the PLE spectrum: the first one was located in the 250–300 nm region and the second one was located in the range of 300–380 nm with a peak at around 347 nm, originating from 4f → 5d transitions of Ce^{3+} ions.[22] The sharp PLE peak at 276 nm was attributed to the $^8S_{7/2} \rightarrow {}^6I_{7/2}$ transition of Gd^{3+} ions, indicating the energy transfer from Gd^{3+} to Ce^{3+} ions in the $Ca_3Gd_{0.99}(AlO)_3(BO_3)_4:0.01Ce^{3+}$ phosphor.[47] The PL spectrum was a broad emission band centered at 402 nm, corresponding to the transition from the 5d level to the ground state of the Ce^{3+} ion.

The PLE and PL spectra of the representative phosphor $Ca_3Gd_{0.95}(AlO)_3(BO_3)_4:0.05Tb^{3+}$ were presented in Fig. 5(b). The PLE spectrum was recorded by monitoring with bright green emission at 544 nm, which revealed a series of excitation bands in the range of 230 to 400 nm. The broad PLE band in the range

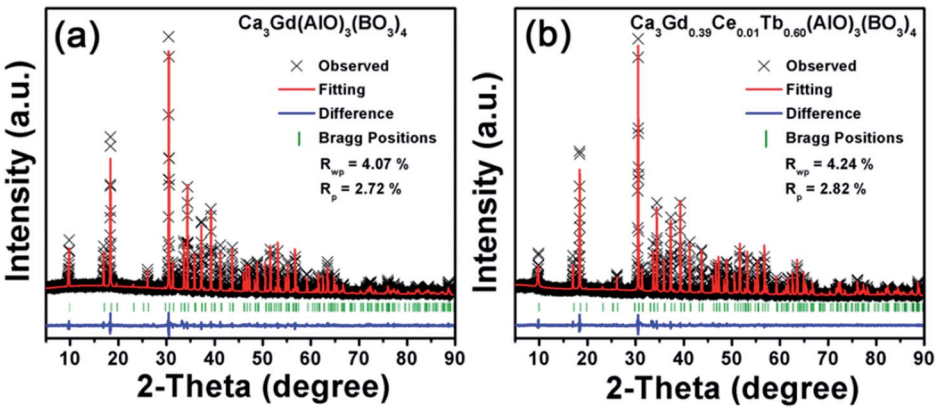

Fig. 2 Rietveld refinements for $Ca_3Gd(AlO)_3(BO_3)_4$ and $Ca_3Gd_{0.39}Ce_{0.01}Tb_{0.6}(AlO)_3(BO_3)_4$.

Table 1 Rietveld refinement results and lattice parameters for $Ca_3Gd(GaO)_3(BO_3)_4$ and $Ca_3Gd_{0.39}Ce_{0.01}Tb_{0.6}(AlO)_3(BO_3)_4$ from the GSAS Rietveld refinement

Formula	$Ca_3Y(AlO)_3(BO_3)_4$	$Ca_3Gd(AlO)_3(BO_3)_4$	$Ca_3Gd_{0.39}Ce_{0.01}Tb_{0.6}(AlO)_3(BO_3)_4$
Crystal system	Hexagonal	Hexagonal	Hexagonal
Space group	*P*63/m	*P*63/m	*P*63/m
2θ-interval,°	10–90	10–90	10–90
a (Å)	10.3877	10.4270	10.4244
b (Å)	10.3877	10.4270	10.4244
c (Å)	5.6920	5.7041	5.7035
V (Å^3)	531.91	537.07	536.75
R_{wp} (%)	—	4.07%	4.24%
R_p (%)	—	2.72%	2.82%

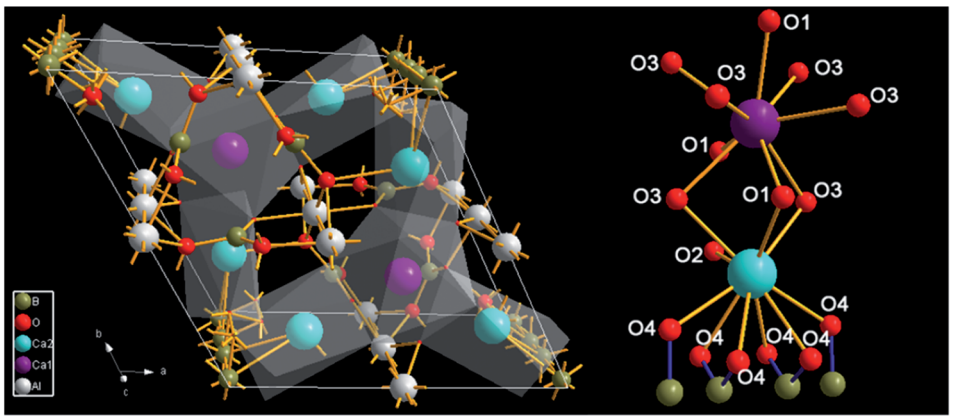

Fig. 3 The crystal of $Ca_3Gd(AlO)_3(BO_3)_4$ and local environment at Ca1 and Ca2 sites.

of 230–300 nm was due to the 4f–5d transitions of Tb^{3+} ions. The PLE peak at 276 nm can be attributed to the $^8S_{7/2} \rightarrow {}^6I_{7/2}$ transition of Gd^{3+} ions, indicating the occurrence of energy transfer from Gd^{3+} to Tb^{3+} ions.[48] In the 300–400 nm wavelength region, a series of PLE peaks were observed, which can be attributed to the 4f–4f electronic transitions of Tb^{3+} ions, such as $^7F_6 \rightarrow {}^5H_7$ at 314 nm, $^7F_6 \rightarrow {}^5L_7$ at 343 nm, $^7F_6 \rightarrow {}^5D_2$ at 352 nm, $^7F_6 \rightarrow {}^5G_6$ at 370 and $^7F_6 \rightarrow {}^5D_3$ at 380 nm. Upon 370 nm excitation, strong green emission was presented in the emission spectrum. The emission peaks at 492, 544, 586, and 622 nm can be assigned to $^5D_4 \rightarrow {}^7F_J$ ($J = 6, 5, 4, 3$) transitions, respectively.[41]

By comparison of the Fig. 5(a) and (b), we can observe the overlap between the emission band of Ce^{3+} and the f–f excitation of Tb^{3+}, indicating the possible resonance energy transfer from Ce^{3+} to Tb^{3+} in $Ca_3Gd(AlO)_3(BO_3)_4$ host. For further identifying it, we measured the PLE and PL spectra of Ce^{3+} and Tb^{3+} co-doped sample $Ca_3Gd_{0.85}(AlO)_3(BO_3)_4$:0.01$Ce^{3+}$,0.05$Tb^{3+}$, as shown in Fig. 5(c). Clearly, not only the characteristic emission bands of Tb^{3+} can be observed under excitation at 347 nm, but

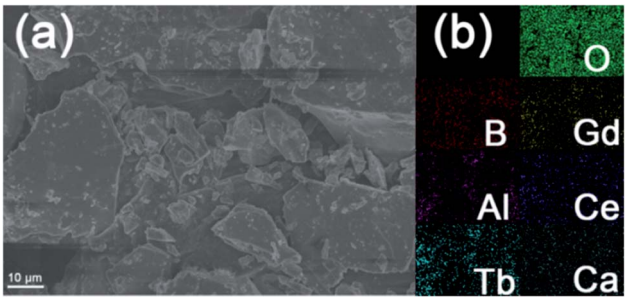

Fig. 4 (a) The SEM and (b) elements mapping of $Ca_3Gd_{0.39}(AlO)_3(BO_3)_4$:0.01$Ce^{3+}$,0.6$Tb^{3+}$.

also the two broad PLE bands of Ce^{3+} also existed when monitored at 544 nm. The results above show the energy transfer from Ce^{3+} to Tb^{3+} truly happened in $Ca_3Gd(AlO)_3(BO_3)_4$ host.

In order to discuss the energy transfer mechanism of Ce^{3+} → Tb^{3+}, the illustration of electronic transitions of Ce^{3+} and Tb^{3+} is depicted in Fig. 6. Under 347 nm excitation, the electrons on Ce^{3+} ions are excited from ground state ($^2F_{7/2}$) to higher excited state (5d), then some excited electrons return to ground states ($^2F_{5/2}$ and $^2F_{7/2}$), generating blue emission of Ce^{3+}. Meanwhile other excited electrons transfer part of their energy from Ce^{3+} 5d level to the excited levels of Tb^{3+} ($^5D_2$) through cross-relaxation, and subsequently, Tb^{3+} relaxes non-radiatively to the $^5D_4$ level from $^5D_2$ and $^5D_3$ states. Finally, radiative transitions take place through $^5D_4$ → ^7F_J (J = 3–6) transitions, giving rise to the characteristic green emissions of Tb^{3+}.

Fig. 7 shows the PL spectra of $Ca_3Gd_{(0.99-x)}(AlO)_3(BO_3)_4$:0.01$Ce^{3+}$,$x$$Tb^{3+}$ (x = 0, 0.02, 0.05, 0.1, 0.2, 0.3, 0.4, 0.5 and 0.6) phosphors under excitation at 347 nm. As can be seen, the PL spectra of Ce^{3+}/Tb^{3+} co-doped $Ca_3Gd(AlO)_3(BO_3)_4$ samples consisted of blue emission band of Ce^{3+} ions and the characteristic green emission peaks of Tb^{3+} ions, due to the energy transfer from Ce^{3+} to Tb^{3+}. Moreover, with increasing Tb^{3+} concentration from x = 0 to x = 0.6, the emission intensity of Ce^{3+} ions decreased monotonically, while the emission intensity of Tb^{3+} ions gradually increased without emission quenching. Interestingly, the emission colour of phosphors can be tuned through increasing Tb^{3+} concentration, and the

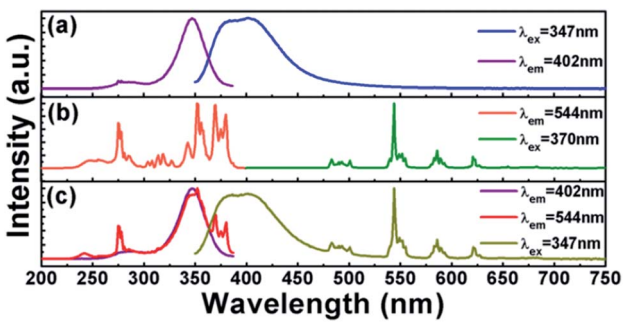

Fig. 5 PLE and PL spectra of (a) $Ca_3Gd_{0.99}(AlO)_3(BO_3)_4$:0.01$Ce^{3+}$, (b) $Ca_3Gd_{0.95}(AlO)_3(BO_3)_4$:0.05$Tb^{3+}$ and (c) $Ca_3Gd_{0.94}(AlO)_3(BO_3)_4$:0.01$Ce^{3+}$,0.05$Tb^{3+}$.

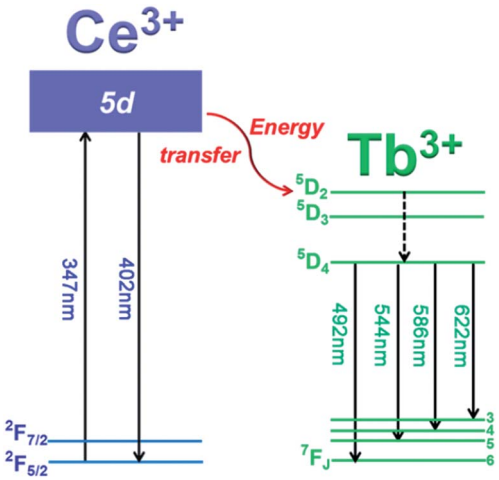

Fig. 6 Illustration of energy levels of Ce^{3+} and Tb^{3+}, and the energy transfer mechanism of Ce^{3+} → Tb^{3+}.

corresponding Commission Internationale de L'Eclairage (CIE) chromaticity moved from blue to green, as can be seen in Fig. 8. The digital photos depict a series of the representative $Ca_3Gd_{(0.99-x)}(AlO)_3(BO_3)_4$:0.01$Ce^{3+}$,$x$$Tb^{3+}$ (x = 0, 0.1, and 0.6) phosphors under 365 nm lamp. These visual images reflect the high potential of the phosphors as luminescence materials in the blue-green emission range. Besides, the IQEs of the $Ca_3Gd_{(0.99-x)}(AlO)_3(BO_3)_4$:0.01$Ce^{3+}$,$x$$Tb^{3+}$ phosphors were also listed in Fig. 8, which can be calculated based on the formula below.[49]

$$\eta_{IQE} = \frac{\int L_S}{\int E_R - \int E_S} \quad (1)$$

where L_S is the emission spectrum of the sample, E_S and E_R represent the excitation light with and without the sample in the integrating sphere, respectively. Herein, the $Ca_3Gd_{0.97}(AlO)_3(BO_3)_4$:0.01$Ce^{3+}$,0.02$Tb^{3+}$ had the maximum value of 55.6%, and the IQE gradually decreased to be 38.2% with the increasing Tb^{3+} concentration x in $Ca_3Gd_{(0.99-x)}(AlO)_3(BO_3)_4$:0.01$Ce^{3+}$,$x$$Tb^{3+}$.

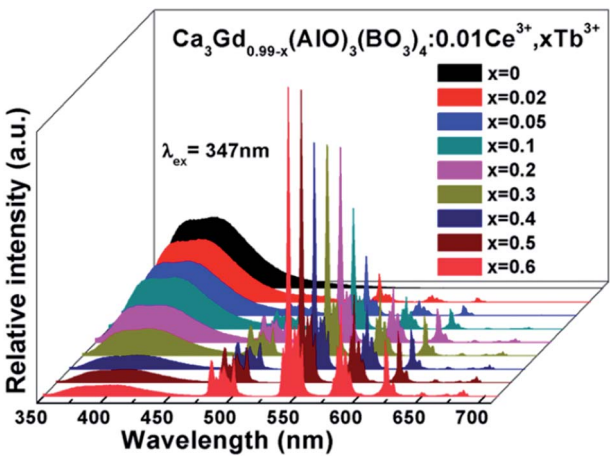

Fig. 7 PL spectra of $Ca_3Gd_{(0.99-x)}(AlO)_3(BO_3)_4$:0.01$Ce^{3+}$,$x$$Tb^{3+}$ (x = 0, 0.02, 0.05, 0.1, 0.2, 0.3, 0.4, 0.5 and 0.6) phosphors excited at 347 nm.

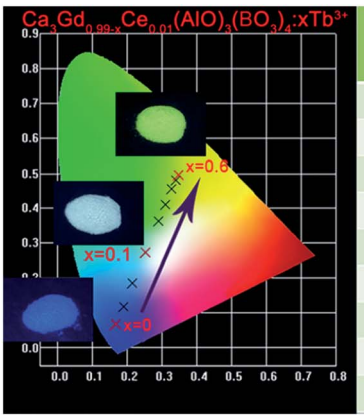

x (mol)	CIE (x, y)	IQE (%)
0	(0.169, 0.067)	48.5
0.02	(0.189, 0.119)	55.6
0.05	(0.216, 0.184)	52.3
0.1	(0.253, 0.272)	50.4
0.2	(0.291, 0.362)	48.5
0.3	(0.309, 0.409)	45.4
0.4	(0.329, 0.456)	42.6
0.5	(0.340, 0.480)	40.2
0.6	(0.347, 0.494)	38.2

Fig. 8 CIE chromaticity diagram showing emission colour tuning in $Ca_3Gd_{(0.99-x)}(AlO)_3(BO_3)_4$:0.01$Ce^{3+}$,x$Tb^{3+}$ phosphors under single 347 nm UV excitation. Insets are photographs of the representative phosphors upon excitation under a 365 nm UV lamp.

3.3 Energy transfer mechanism

The decay curves of $Ca_3Gd_{(0.99-x)}(AlO)_3(BO_3)_4$:0.01$Ce^{3+}$,x$Tb^{3+}$ samples were measured for identifying the energy transfer mechanism, as shown in Fig. 9. The fluorescence average lifetimes τ can be obtained from following formula:

$$I(t) = I_1 \exp\left(-\frac{t}{\tau_1}\right) + I_2 \exp\left(-\frac{t}{\tau_2}\right) \quad (2)$$

where I_1 and I_2 refer to intensities at different time, and τ_1 and τ_2 represent the corresponding decay time for the exponential components, respectively. The obtained average decay lifetimes of Ce^{3+} are determined to be 29.47, 28.93, 28.00, 26.42, 24.31, 21.61, 19.03, 17.07 and 15.76 ns with increasing contents of Tb^{3+} ions from $x = 0$ to $x = 0.6$. Obviously, the lifetime gradually decreased with increasing Tb^{3+} concentration, confirming the above-mentioned energy transfer mechanism of $Ce^{3+} \rightarrow Tb^{3+}$. The energy transfer efficiency (η_T) of $Ce^{3+} \rightarrow Tb^{3+}$ can be obtained using the equation below:[42]

$$\eta_T = 1 - \frac{I_S}{I_{S0}} \quad (3)$$

where I_{S0} and I_S represent the luminescence intensity of $Ca_3Gd_{0.99}(AlO)_3(BO_3)_4$:0.01$Ce^{3+}$ and $Ca_3Gd_{(0.99-x)}(AlO)_3(BO_3)_4$:0.01$Ce^{3+}$,x$Tb^{3+}$ ($x = 0.02$, 0.05, 0.1, 0.2, 0.3, 0.4, 0.5 and 0.6). According to the dependence of the intensities of the 5d–4f transition of Ce^{3+} at 402 nm, the energy transfer efficiency of $Ce^{3+} \rightarrow Tb^{3+}$ was calculated and shown in Fig. 10. At the beginning of the process, the energy transfer efficiency raised rashly with increasing Tb^{3+} concentration. Subsequently, it grew slowly after $x = 0.4$, and eventually reached up to 83.6% when $x = 0.6$.

As it is known, the mechanism of energy transfer from Ce^{3+} to Tb^{3+} ions can be attributed to exchange interaction or electric multipolar interaction. To figure out which interaction dominated in the energy transfer process, the average distance (R_c) between the Ce^{3+} donors and Tb^{3+} acceptor ions in $Ca_3Gd_{0.39}(AlO)_3(BO_3)_4$:0.01$Ce^{3+}$,0.6$Tb^{3+}$ phosphor was evaluated by using the following equation:[21]

$$R_c = 2\left[\frac{3V}{4\pi CN}\right]^{\frac{1}{3}} \quad (4)$$

where C is the total concentration of Ce^{3+} and Tb^{3+} ions, N is coordination number, and V is the cell volume. For the $Ca_3Gd_{0.39}(AlO)_3(BO_3)_4$:0.01$Ce^{3+}$,0.6$Tb^{3+}$ phosphor, the V, C and N are 536.75 Å^3, 0.61 and 2, respectively. Accordingly, R_c was determined to be 9.44 Å. Generally, exchange interaction

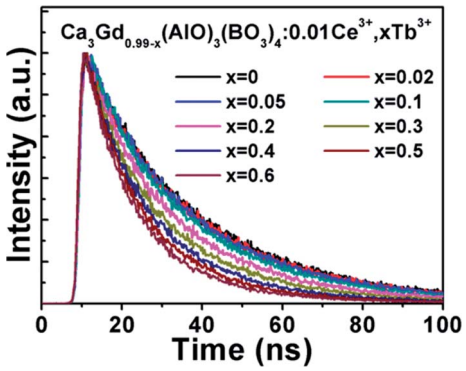

Fig. 9 Fluorescence decay curves of Ce^{3+} in $Ca_3Gd_{(0.99-x)}(AlO)_3(BO_3)_4$:0.01$Ce^{3+}$,x$Tb^{3+}$ after pulse excitation at 347 nm while monitored at 402 nm.

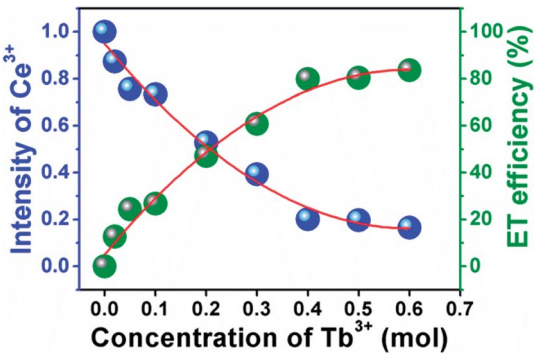

Fig. 10 Dependence of Ce^{3+} emission intensities and energy transfer efficiency on Tb^{3+} concentration in $Ca_3Gd_{(0.99-x)}(AlO)_3(BO_3)_4$:0.01$Ce^{3+}$,x$Tb^{3+}$.

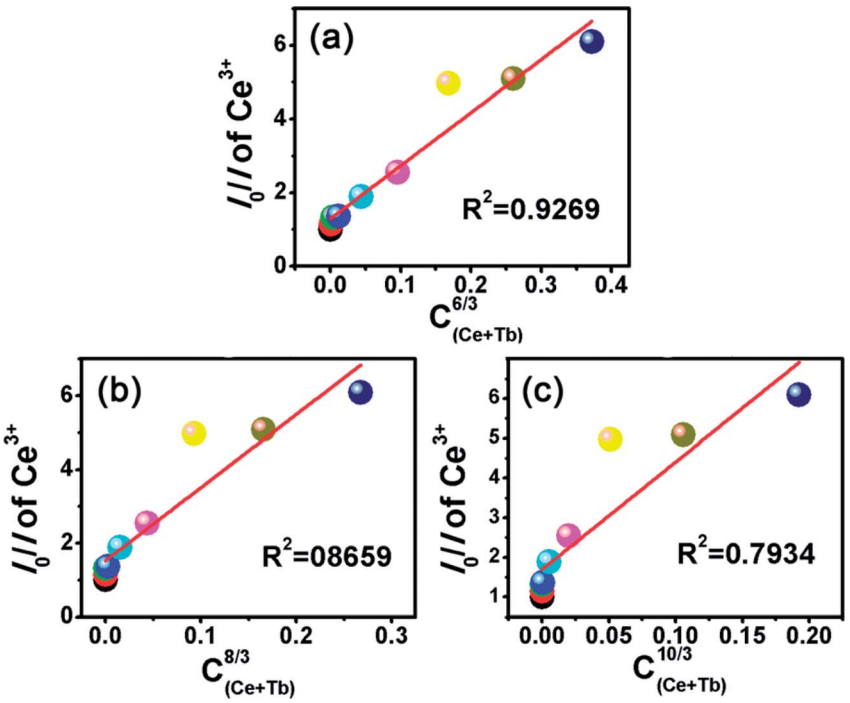

Fig. 11 Dependence of I_0/I on (a) $C_{(Ce+Tb)}{}^{6/3}$, (b) $C_{(Ce+Tb)}{}^{8/3}$ and (c) $C_{(Ce+Tb)}{}^{10/3}$.

requires a smaller R_c value (<5 Å),[15] and consequently the energy transfer from Ce^{3+} to Tb^{3+} in $Ca_3Gd_{0.39}(AlO)_3(BO_3)_4$:0.01-$Ce^{3+}$,0.6$Tb^{3+}$ phosphor would take place *via* electric multipolar interaction.

As discussed by many researchers, the multipolar interaction can be further confirmed by using the following formula:[38]

$$\eta_0/\eta \propto C^{\frac{n}{3}} \quad (5)$$

where η_0 and η are the QEs of the Ce^{3+} in the absence and presence of Tb^{3+}, respectively. The value of η_0/η can be approximately calculated by the ratio of relative luminescence intensity ratio (I_{S0}/I); C is the concentration of the sum of Ce^{3+} and Tb^{3+}. By using eqn (5), the electric multipolar interaction parameter n taking the values 6 (dipole–dipole), 8 (dipole–quadrupole), and 10 (quadrupole–quadrupole) were compared by the dependence of I_{S0}/I of Ce^{3+} on $C^{n/3}$, as demonstrated in Fig. 11. A line relation was well-fitted at $n = 6$, so the energy-transfer mechanism of $Ce^{3+} \rightarrow Tb^{3+}$ could be the dipole–dipole interaction.

3.4 Thermal stability

As a very important index, the thermal stability can influence the colour output and brightness of phosphor. Therefore, we measured the temperature-dependent emission spectra of $Ca_3Gd_{0.39}(AlO)_3(BO_3)_4$:0.01$Ce^{3+}$,0.6$Tb^{3+}$ sample and the curves were shown in Fig. 12(a). Clearly, with temperature increased from 303 K to 523 K, the emission intensity of $Ca_3Gd_{0.39}$-

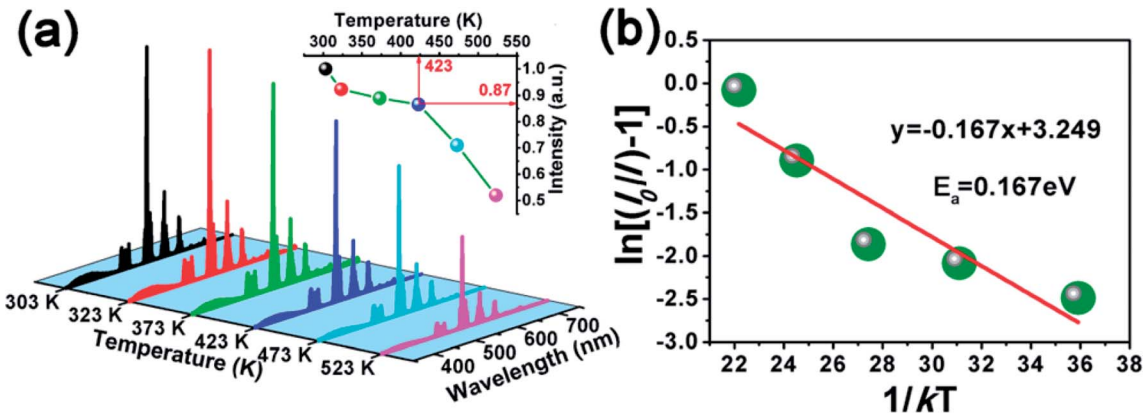

Fig. 12 (a) Temperature-dependent PL spectra of $CaGd_{0.39}(AlO)_3(BO_3)_4$:0.01$Ce^{3+}$,0.6$Tb^{3+}$ phosphor excited at 347 nm. The inset shows normalized PL emission intensity of $CaGd_{0.39}(AlO)_3(BO_3)_4$:0.01$Ce^{3+}$,0.6$Tb^{3+}$ phosphor as a function of temperature. (b) Plot of $\ln(I_0/I - 1)$ *versus* $1/kT$ and the calculated activation energy (E_a) for the phosphor.

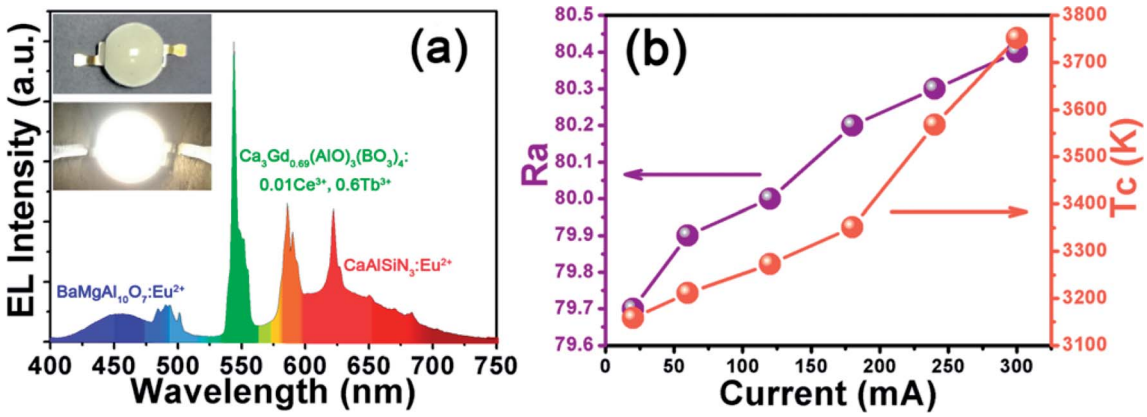

Fig. 13 (a) EL spectrum of the fabricated WLED lamp with 365 nm NUV chip and $BaMgAl_{10}O_7:Eu^{2+}$, $CaAlSiN_3:Eu^{2+}$ and $CaGd_{0.39}(AlO)_3(BO_3)_4$:0.01$Ce^{3+}$,0.6$Tb^{3+}$ phosphors driven by 120 mA current. (b) The variation of R_a and T_c on different driven currents.

$(AlO)_3(BO_3)_4$:0.01Ce^{3+},0.6Tb^{3+} decreased due to thermal quenching but still maintained the same profiles. Surprisingly, the PL intensity at 423 K was about 87% of that at 303 K, demonstrating that $Ca_3Gd_{0.39}(AlO)_3(BO_3)_4$:0.01$Ce^{3+}$,0.6$Tb^{3+}$ phosphor possessed superior thermal stability and thus it suits for fabricating WLEDs.

The modified Arrhenius equation was then used to fit the thermal quenching data for activation energy calculation:[50]

$$\frac{I_T}{I_0} = \left[1 + C\exp\left(\frac{E_a}{kT}\right)\right]^{-1} \quad (6)$$

in which I_0 is the initial emission intensity, I_T is the intensity at temperature T, E_a is the activation energy, C is a constant for a certain host and k is the Boltzmann constant, respectively. Fig. 12(b) shows the plot of $\ln(I_0/I - 1)$ *vs.* $1/kT$, and the experimental data can be linear fitted with a slope of −0.167. Thus, the activation energy of thermal quenching was 0.167 eV.

3.5 Electroluminescence properties of WLEDs fabricated with $Ca_3Gd_{0.39}(AlO)_3(BO_3)_4$:0.01$Ce^{3+}$,0.6$Tb^{3+}$

In order to evaluate the potential application of $Ca_3Gd_{0.39}(AlO)_3(BO_3)_4$:0.01$Ce^{3+}$,0.6$Tb^{3+}$ phosphor, a WLED lamp was fabricated through the combined use of a NUV chip (365 nm) and $BaMgAl_{10}O_7:Eu^{2+}$ blue phosphor, $CaAlSiN_3:Eu^{2+}$ red phosphor and $Ca_3Gd_{0.39}(AlO)_3(BO_3)_4$:0.01$Ce^{3+}$,0.6$Tb^{3+}$ green phosphor driven by a 20 mA current. The electroluminescence (EL) spectrum of such a WLED under the driven current of 20 mA was shown in Fig. 13(a). The bright warm white light can be seen in the inset of Fig. 13(a). The CCT, CRI (Ra), and CIE chromaticity coordinate of this WLED device was measured to be 3158 K, 79.7, and (0.427, 0.401), respectively. The above values of the WLED device under various currents were also measured (see Fig. 13(b)) and there was little variation, which confirmed the stable white light output in the device.

4. Conclusions

In summary, we have successfully developed a novel green emitting phosphor for near UV-pumped WLEDs. The energy transfer from Ce^{3+} to Tb^{3+} in $Ca_3Gd(AlO)_3(BO_3)_4$ host has been demonstrated to be the dipole–dipole interaction, and the energy transfer efficiency was as high as 83.6% on $Ca_3Gd_{0.39}(AlO)_3(BO_3)_4$:0.01$Ce^{3+}$,0.6$Tb^{3+}$. The energy transfer critical distance was calculated to be 9.44 Å according to the concentration quenching method. The emission colour of the obtained phosphors can be tuned appropriately from deep blue (0.169, 0.067) to green (0.347, 0.494) by increasing the contents of Tb^{3+} ions. Besides, $Ca_3Gd_{0.39}(AlO)_3(BO_3)_4$:0.01$Ce^{3+}$,0.6$Tb^{3+}$ phosphor possessed good thermal stability at high temperature, and the emission intensity at 423 K was about 87% of that at 303 K. A prototype LED device was fabricated by using the $BaMgAl_{10}O_7:Eu^{2+}$ blue phosphor, $CaAlSiN_3:Eu^{2+}$ red phosphor and $Ca_3Gd_{0.39}(AlO)_3(BO_3)_4$:0.01$Ce^{3+}$,0.6$Tb^{3+}$ green phosphor and 365 nm-emitting InGaN chip, and bright warm white light with CCT (3158 K), CRI (79.7), and CIE chromaticity coordinates (0.427, 0.401) was achieved. These results indicate that the $Ca_3Gd_{0.39}(AlO)_3(BO_3)_4$:0.01$Ce^{3+}$,0.6$Tb^{3+}$ sample can be as a promising green-emitting phosphor for UV-based white LEDs.

Conflicts of interest

There are no conflicts to declare.

Acknowledgements

This work was supported by the National Natural Science Foundation of China (No. 51502190), the Program for the Outstanding Innovative Teams of Higher Learning Institutions of Shanxi, the Start-up Research Grant of Taiyuan University of Technology (No. Tyutrc201489a), the Excellent Young Scholars Research Grant of Taiyuan University of Technology (No. 2014YQ009, 2015YQ006, and 2016YQ03), and the Open Fund of the State Key Laboratory of Luminescent Materials and Devices (South China University of Technology, No. 2017-skllmd-01).

References

1 W. B. Dai, Y. F. Lei, J. Zhou, M. Xu, L. L. Chu, L. Li, P. Zhao, Z. H. Zhang, W. B. Dai and Y. F. Lei, *J. Alloys Compd.*, 2017, **726**, 230–239.
2 W. B. Dai, Y. F. Lei, J. Zhou, Y. Zhao, Y. H. Zheng, M. Xu, S. L. Wang and F. Shen, *J. Am. Ceram. Soc.*, 2017, **100**, 5174–5185.
3 P. Du, X. Huang and J. S. Yu, *Inorg. Chem. Front.*, 2017, **4**, 1987–1995.
4 X. Huang, *J. Alloys Compd.*, 2015, **628**, 240–244.
5 X. Huang, *Opt. Lett.*, 2015, **40**, 3599–3602.
6 X. Huang, *Dyes Pigm.*, 2016, **130**, 99–105.
7 X. Huang, S. Han, W. Huang and X. Liu, *Chem. Soc. Rev.*, 2013, **44**, 173–201.
8 X. Y. Huang, X. H. Ji and Q. Y. Zhang, *J. Am. Ceram. Soc.*, 2011, **94**, 833–837.
9 B. Shao, Z. W. Yang, Y. D. Wang, J. Li, J. Z. Yang, J. B. Qiu and Z. G. Song, *ACS Appl. Mater. Interfaces*, 2015, **7**, 25211–25218.
10 X. Huang, *Nat. Photonics*, 2014, **8**, 748–749.
11 X. Y. Huang and J. Lin, *J. Mater. Chem. C*, 2015, **3**, 7652–7657.
12 X. Huang, *J. Alloys Compd.*, 2017, **690**, 356–359.
13 P. Du, X. Huang and J. S. Yu, *Chem. Eng. J.*, 2018, **337**, 91–100.
14 F. Kang, M. Peng, D. Y. Lei and Q. Zhang, *Chem. Mater.*, 2016, **28**, 7807–7815.
15 F. Kang, H. Zhang, L. Wondraczek, X. Yang, Y. Zhang, D. Y. Lei and M. Peng, *Chem. Mater.*, 2016, **28**, 2692–2703.
16 J. Han, L. Li, M. Peng, B. Huang, F. Pan, F. Kang, L. Li, J. Wang and B. Lei, *Chem. Mater.*, 2017, **29**, 8412–8424.
17 P. Du, L. Luo, H. K. Park and J. S. Yu, *Chem. Eng. J.*, 2016, **306**, 840–848.
18 P. Du and J. S. Yu, *Chem. Eng. J.*, 2017, 327.
19 P. Du and J. S. Yu, *Sci. Rep.*, 2017, **7**, 11953.
20 C. H. Huang and T. M. Chen, *J. Phys. Chem. C*, 2011, **115**, 2349–2355.
21 B. Li and X. Huang, *Ceram. Int.*, 2018, **44**, 4915–4923.
22 F. W. Kang, L. J. Li, J. Han, D. Y. Lei and M. Y. Peng, *J. Mater. Chem. C*, 2017, **5**, 390–398.
23 J. Zhao, C. F. Guo, T. Li, X. Y. Su, N. M. Zhang and J. Y. Chen, *Dyes Pigm.*, 2016, **132**, 159–166.
24 Z.-C. Wu, F.-F. Wang, K. Zhang, S.-C. Xu, J. Liu, Z. Xia and M.-M. Wu, *Dyes Pigm.*, 2017, **150**, 275–283.
25 M. Shang, S. Liang, H. Lian and J. Lin, *Inorg. Chem.*, 2017, **56**, 6131.
26 M. Shang, C. Li and J. Lin, *Chem. Soc. Rev.*, 2014, **43**, 1372–1386.
27 M. Y. Peng, X. W. Yin, P. A. Tanner, M. G. Brik and P. F. Li, *Chem. Mater.*, 2015, **27**, 2938–2945.
28 Z. Mao, J. Chen, L. Jian and D. Wang, *Chem. Eng. J.*, 2016, **284**, 1003–1007.
29 G. Li, J. Chen, Z. Mao, W. Song, T. Sun and D. Wang, *Ceram. Int.*, 2016, **42**, 1756–1761.
30 X. Huang, H. Guo and B. Li, *J. Alloys Compd.*, 2017, **720**, 29–38.
31 L. Huang, Y. Zhu, X. Zhang, R. Zou, F. Pan, J. Wang and M. Wu, *Chem. Mater.*, 2016, **28**, 1495–1502.
32 P. Du and J. S. Yu, *Dyes Pigm.*, 2017, **147**, 16–23.
33 P. Du, L. K. Bharat and J. S. Yu, *J. Alloys Compd.*, 2015, **633**, 37–41.
34 W. Dai, Y. Lei, M. Xu, P. Zhao, Z. Zhang and J. Zhou, *Sci. Rep.*, 2017, **7**, 12872.
35 R. P. Cao, Y. J. Ye, Q. Y. Peng, G. T. Zheng, H. Ao, J. W. Fu, Y. M. Guo and B. Guo, *Dyes Pigm.*, 2017, **146**, 14–19.
36 R. Cao, C. Liao, F. Xiao, G. Zheng, W. Hu, Y. Guo and Y. Ye, *Dyes Pigm.*, 2018, **149**, 574–580.
37 R. Cao, T. Fu, Y. Cao, H. Ao, S. Guo and G. Zheng, *Mater. Lett.*, 2015, **155**, 68–70.
38 B. Li, X. Huang, H. Guo and Y. Zeng, *Dyes Pigm.*, 2018, **150**, 67–72.
39 A. Huang, Z. Yang, C. Yu, Z. Chai, J. Qiu and Z. Song, *J. Phys. Chem. C*, 2017, 121.
40 C. Y. Yu, Z. W. Yang, A. J. Huang, Z. Z. Chai, J. B. Qiu, Z. G. Song and D. C. Zhou, *J. Non-Cryst. Solids*, 2017, **457**, 1–8.
41 X. Y. Huang, B. Li and H. Guo, *J. Alloys Compd.*, 2017, **695**, 2773–2780.
42 H. Guo, B. Devakumar, B. Li and X. Huang, *Dyes Pigm.*, 2018, **151**, 81–88.
43 M. Wen, H. Wu, X. Su, J. Lu, Z. Yang, X. Wu and S. Pan, *Dalton Trans.*, 2017, **46**, 4968–4974.
44 J. T. Ingle, A. B. Gawande, R. P. Sonekar, S. K. Omanwar, Y. Wang and L. Zhao, *J. Alloys Compd.*, 2014, **585**, 633–636.
45 R. D. Shannon, *Acta Crystallogr.*, 1976, **32**, 751–767.
46 Y. Yu, Q. S. Wu and R. K. Li, *J. Solid State Chem.*, 2006, **179**, 429–432.
47 E. J. Bosze, G. A. Hirata, L. E. Shea-Rohwer and J. Mckittrick, *J. Lumin.*, 2003, **104**, 47–54.
48 Y. C. Li, Y. S. Chang, Y. C. Lai, Y. J. Lin, C. H. Laing and Y. H. Chang, *Mater. Sci. Eng., B*, 2007, **146**, 225–230.
49 J. Zhong, D. Chen, H. Xu, W. Zhao, J. Sun and Z. Ji, *J. Alloys Compd.*, 2017, **695**, 311–318.
50 X. Huang, B. Li, H. Guo and D. Chen, *Dyes Pigm.*, 2017, **143**, 86–94.

